Materials Research Bulletin 164 (2023) 112252

Contents lists available at ScienceDirect

Materials Research Bulletin

journal homepage: www.elsevier.com/locate/matresbu

Research Papers

Disclosing the nature of vacancy defects in α-Ag_2WO_4

M. Assis [a,b,*], M.S. Castro [c], C.M. Aldao [d], C. Buono [d], P.P. Ortega [e], M.D. Teodoro [f], J. Andrés [b], A.F. Gouveia [b], A.Z. Simões [e], E. Longo [a], C.E. Macchi [g], A. Somoza [g], F. Moura [h], M.A. Ponce [a,c,h]

[a] CDMF, Federal University of São Carlos (UFSCar), São Carlos 13565-905, Brazil
[b] Department of Physical and Analytical Chemistry, University Jaume I (UJI), Castellón 12071, Spain
[c] Institute of Materials Science and Technology (INTEMA), University of Mar del Plata and National Research Council (CONICET), Av. Colón 10850, Mar del Plata B7606 FWV, Argentina
[d] Institute of Scientific and Technological Research in Electronics (ICYTE), University of Mar del Plata and National Research Council (CONICET), Juan B. Justo 4302, Mar del Plata B7608FDQ, Argentina
[e] School of Engineering, São Paulo State University (UNESP), Av. Dr. Ariberto Pereira da Cunha 333, Portal das Colinas, Guaratinguetá 12516-410, Brazil
[f] Department of Physics, Federal University of São Carlos (UFSCar), São Carlos 13565-905, Brazil
[g] Institute of Materials Physics of Tandil - IFIMAT (UNCPBA) and CIFICEN (UNCPBA-CICPBA-CONICET), Pinto 399, Tandil B7000GHG, Argentina
[h] Advanced Materials Interdisciplinary Laboratory, Federal University of Itajubá, Unifei – Campus Itabira, MG, Brazil

ARTICLE INFO

Keywords:
α-Ag_2WO_4
Defects
Electronic properties

ABSTRACT

Defects at semiconductors with electron acceptor and donor sites govern the electronic and optoelectronic applications due to their unique electronic properties. This work provides deep insight into the nature of defects and the conduction mechanism in α-Ag_2WO_4. To this aim, a detailed analysis of the results of XRD with Rietveld refinements, FE-SEM images, and measurements of different spectroscopies (impedance, positron annihilation lifetime, and photoluminescence) are carried out on α-Ag_2WO_4 samples synthesized by a simple co-precipitation method. Two types of vacancy defects: cationic O-vacancies, and anionic Ag or Ag–O vacancy complexes are elucidated with a Schottky p-type potential barrier. The results indicate that the Ag vacancies remain constant during thermal treatment, while an opposite effect is found for the oxygen vacancies. This behavior governs the multifunctional properties of α-Ag_2WO_4 semiconductors via a tunneling plus thermionic conduction mechanism.

1. Introduction

The rapid progress in semiconductor nanotechnology relies on three factors: (i) the success in quantifying and understanding the amount and nature of defects, (ii) the employment of appropriate synthetic procedures to control the presence of defects, and (iii) adequate post-physical modifications to obtain high-quality of crystals that possess unique and extraordinary properties [1–6]. Semiconductors formed after the synthesis process and thermal treatment contain defects owing to the reaction process, which inevitably exist and alter the properties.

Defects are general perturbations of the periodic atomic arrangements in semiconductor materials. They are known to manifest themselves as energy levels, within the band gap, tuning the physicochemical properties by changing the electrical features with enhanced or novel functional applications. In this sense, it is essential to understand the nature and influence of defects on the activity and performance for further optimization of the semiconductor system. In transition metal oxides, defects can be associated with cationic vacancies (oxygen vacancies, V_O) and anionic vacancies (silver vacancies or vacancy complexes, $V_{Ag\text{-}O}$) [7]. These vacancies act not only as an electron-hole recombinant center capturing a free electron and a free hole, but also break the electronic structure of an otherwise perfectly periodic crystal. Recently, it has been found that the presence of V_O provokes the formation of reactive sites in these semiconductors, which can promote the migration of these carriers and reduce the interfacial reaction energy barrier [8–12]. The spatial distribution of V_O dictates its nature while the surrounding atoms are re-organized for defect energy level formation. Control and manipulation of defects provide a degree of freedom for harvesting and tailoring the functional properties of semiconductors. However, the rapid and simple detection of V_O is a great challenge owing to its elusive and highly diluted contents.

Transition-metal tungstates have recently gained significant attention in the scientific community owing to their excellent and favorable properties that are applied in photocatalysts, gas sensors, lasers, and

* Corresponding author at: CDMF, Federal University of São Carlos (UFSCar), São Carlos 13565-905, Brazil.
E-mail address: marcelostassis@gmail.com (M. Assis).

https://doi.org/10.1016/j.materresbull.2023.112252
Received 3 October 2022; Received in revised form 16 March 2023; Accepted 26 March 2023
Available online 27 March 2023

supercapacitors [13–15]. Silver tungstate (α-Ag_2WO_4) is a representative member of this family with remarkable physical/chemical properties that mainly depend on the intrinsic defects controlling their structure and electronic properties, and advanced applications such as antimicrobial, photocatalyst, gas sensor, and antitumoral [15–18]. α-Ag_2WO_4 presents a unique atomic arrangement that provides a fundamental ability to accommodate a large number of defects without destabilizing the crystal structure. Significantly, the properties of α-Ag_2WO_4 are highly tunable by selecting the temperature, pH, pressure, type of solvent, and surfactant along the synthesis process [19]. The unique structure of α-Ag_2WO_4 and electronic flexibility allows the substitution of Ag atoms by different transition metals, such as Zn, Cu, Mn, and Ni atoms, and/or W by Mo cations to form solid solutions with enhanced photocatalytic performance [20–24]. In addition, the doping of α-Ag_2WO_4 with rare earth cations renders materials with interesting photoluminescence (PL) emissions [25,26]. In this scenario, our group is engaged in a research project devoted to understanding the nature of the defects in semiconductors, and very recently, we have been employing positron annihilation lifetime spectroscopy (PALS) to establish the nature of vacancy-like defects in both pure α-Ag_2WO_4 samples and those submitted to electron beam irradiation [27].

Here, we report the controlled synthesis of polycrystalline α-Ag_2WO_4 by using the co-precipitation (CP) method, free of any template and without surfactants. Impedance spectroscopy has been applied, for the first time, to unveil the nature of the defects. The obtained material was characterized by Rietveld refinement and field emission scanning electron microscopy (FE-SEM), PALS measurements, and PL emissions. The main aims are fourth fold: (i) disclose the nature of defects at the α-Ag_2WO_4 semiconductor; (ii) understand the dependence of the concentration of these defects as a function of temperature treatment; (iii) find a relationship among PL emissions, PALS measurements, and results of the impedance spectroscopy; and (iv) propose a plausible mechanism for the conduction behavior based on present findings.

2. Experimental procedures

2.1. Synthesis and characterization

The α-Ag_2WO_4 powder was synthesized by using the CP method as described in the literature [27]. The α-Ag_2WO_4 pellet was obtained by cold pressing the α-Ag_2WO_4 powder at a pressure of 1 atm for 5 min and 70 °C. The pellets were characterized by X-ray diffraction (XRD) using the D/Max-2500 PC diffractometer (Rigaku, Japan) with the CuKα radiation ($\lambda = 1.5406$ Å) in the 2θ range (10° - 110°) at the rate of 1°/min. The Rietveld refinements were performed using the General Structure Analysis System (GSAS). The morphology of the α-Ag_2WO_4 powder was observed with an FE-SEM Supra 35-VP (Carl Zeiss, Germany) operated at 5 kV. Room-temperature PL measurements were performed using as an excitation source a 355 nm laser (Cobol/Zouk) focused on a 200 μm spot with a constant power of 5 mW. The luminescence signal was dispersed by a 19.3 cm spectrometer (Andor/Kymera) and detected by a Si charge-coupled device. For PL measurements samples were treated at the same temperature steps of the impedance spectroscopy analysis.

2.2. Direct current (DC) semiconductor characterization

To determine the semiconductor behavior (*n*- or p-type) of the α-Ag_2WO_4 pellets with thermal treatment, thick films were conformed and treated in three different atmospheres (vacuum, oxidant, and reductive). The measurements were carried out at 150 °C, and an excitation current of 1 mA was applied by using a two-point probe technique with a DC-type measurement. An Agilent 3440A multimeter was employed for the electrical conductance measurements.

2.3. PALS measurements

Positron annihilation lifetime measurements were performed using a fast−fast spectrometer with a time resolution of 251 ps in a collinear geometry. A 10 μCi-sealed source of ^{22}NaCl deposited onto two thin Kapton foils (7.5 μm thick) sandwiched between two identical samples was used as a positron source. The spectra were recorded at room temperature, and typical $1.5 - 2 \times 10^6$ counts per spectrum were collected. The lifetime values reported in this work for each sample are at least an average of 10 measurements in the same experimental conditions. After subtracting the background and the source contribution, the PALS spectra were analyzed using the LT10 program [28].

In general, from the positron lifetime spectra decomposition, several lifetime components can be extracted; each of them is characterized by a lifetime τ_i and an associated intensity I_i. The state *i* can be the delocalized one in the crystal lattice (free positron state) or localized states at different defect sites where positrons become trapped and annihilated. The presence of more than one lifetime indicates that the studied sample is not defect-free, which is common in semiconductor oxide samples. PALS measurements were performed to establish if the defect structure of the α-Ag_2WO_4 compound was modified when this sample was submitted to the same thermal treatment used for the impedance spectroscopy measurements; specifically, the sample was *ex-situ* heated from 303 up to 423 K at a heating rate of 1 K/min and then maintained at this temperature for 30 min. Detailed analysis of the PALS measurements performed is presented in the supporting information (Fig. SI-1).

2.4. Impedance spectroscopy

The impedance spectroscopy technique provides fundamental characteristics of semiconductors like conductivity (σ) as a function of time, temperature, applied voltage bias, and frequency (ω) [29,30]. Impedance measurements were carried out with an HP 4284A LRC meter. The measurement frequency range was from 100 Hz to 1 MHz. The impedance data have been measured in the temperature range between 303 and 423 K with an increasing rate of ~1 K/min. To ensure that the system is in a steady state previously to the data acquisition, the temperature was kept constant at a predetermined value until it did not vary with time. For each temperature, a sequential number of measurements were performed, and the capacitances and electrical resistances were estimated by fitting the data to an equivalent circuit using Zview 2.1 software. The relative error for all measurements was lower than 3%.

3. Results and discussion

An analysis of the XRD data (Fig. SI-2) renders that all samples have well-defined diffraction peaks, indicating a good degree of structural order. The as-synthesized α-Ag_2WO_4 samples present an orthorhombic structure belonging to the symmetry *Pn*2*n* space group, according to card No. 4165 in the *Inorganic Crystal Structure Database* (ICSD). The results of Rietveld refinements are presented in Fig. SI-3 and Table SI-1. An analysis of the results renders that, after thermal treatment, there is a slight increase in the lattice parameters of the crystalline cell. The α-Ag_2WO_4 powder observed with an FE-SEM was the rod-like morphology as reported in the literature (see Fig. SI-4).

3.1. Two-point probe DC measurements

Fig. 1A is a schematic representation of a semiconductor's electrical behavior when acts as an *n*- or p-type semiconductor. Reducing gasses, such as CO, react and then remove ionosorbed oxygen from the surface. Thus, electrons returned to the grains. In general, for an n-type semiconductor, this implies lower intergranular barriers, and then the film conductivity increases (resistivity decreases). The opposite behavior is expected when a p-type semiconductor is exposed to air, for which intergranular barriers decrease and the conductivity increases

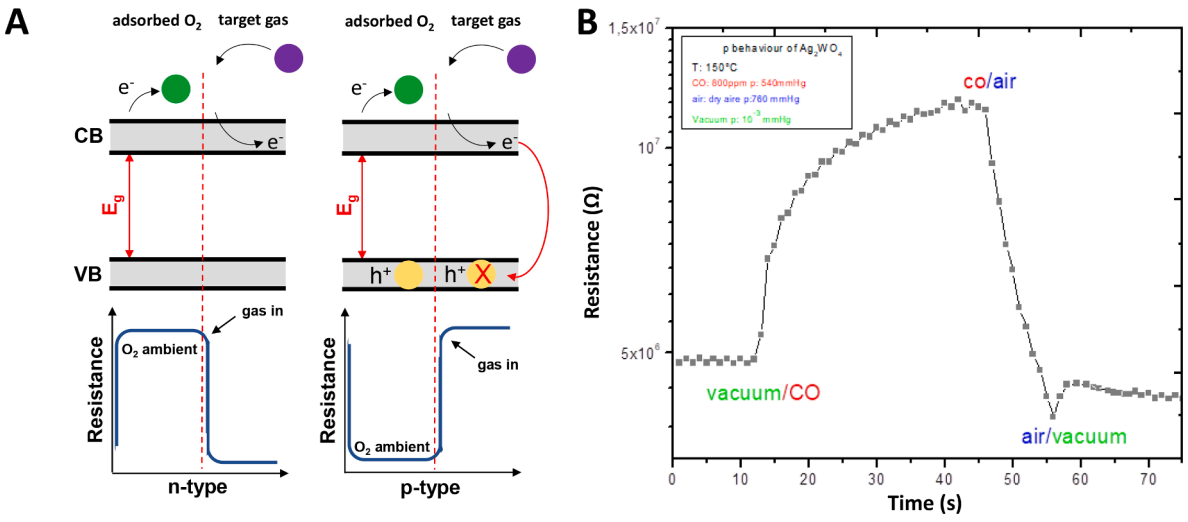

Fig. 1. **(A)** Schematic representation of the electrical behavior when the material acts as an *n*- or p-type semiconductor when it is exposed to a reducing gas (target gas). **(B)** Electrical behavior of α-Ag_2WO_4 film.

(resistivity decreases). In Fig. 1B, the time response of the α-Ag_2WO_4 film is presented. Measurements were carried out when samples were heated at 423 K. Time response results show that after a quick resistance increase due to the change from vacuum to CO exposure, a decrease in the electrical resistance is observed when samples were exposed to air. A reproducible behavior is observed for CO and air exposures indicating a p-type behavior where the resistance increases after the air removal. This experimental result is in agreement with the p-type behavior predicted previously by our research group [31] based on first-principles calculations.

N_A and N_D correspond to the concentration of acceptor and donor impurities, respectively, being $N{=}N_A - N_D$, the net acceptor concentration. The band diagram at the grain surface adopts the form shown in Fig. SI-5.

3.2. PALS analysis

To analyze the temperature effects on the defects, PALS measurements were performed to establish if the defect structure of the α-Ag_2WO_4 compound was modified when this sample was submitted to the same thermal treatment used along the impedance spectroscopy measurements. The measured positron lifetime spectra could be satisfactorily fitted considering three discrete lifetime components. In both samples, the intensity associated with the longest lifetime component (τ_3~1800 ps), usually ascribed to the annihilation via the pickoff process of the ortho-Positronium atom formed in the intergranular spaces of the powder samples, is lower than 3% [32]. Taking into account the small value of its intensity, this lifetime component is not discussed further. The obtained results for the other two lifetime components are presented in Table 1.

As can be seen in the table, the values of the positron parameters obtained from PALS measurements in the thermally treated sample are the same, within the experimental error, that those already reported for a non-heated α-Ag_2WO_4 sample [27]. The values of **τ** and I are maintained along thermal treatments. Specifically, it was pointed out that the positron trapping sites are V_{Ag} or $V_{Ag\text{-}O}$ vacancy complexes characterized by a positron lifetime $\tau_2 = 274{\pm}2$ ps. Furthermore, the value of the intensity associated with this lifetime component (I_2 ~73%) indicated the presence of a high concentration of this type of defect. It is worth mentioning that isolated oxygen vacancies (V_O) are invisible to positrons. In fact, due to their positive charge, these defects repel positrons, making them not effective positron traps [33]. Therefore, PALS results indicate that, during the impedance spectroscopy measurements, the number of Ag–O vacancy complexes does not change.

Table 1
Values of positron lifetimes (**τ**) and their associated intensities (I) obtained from the decomposition of PALS spectra for α-Ag_2WO_4 samples before and after the thermal treatment used for the impedance spectroscopy measurements.

α-Ag_2WO_4 samples' state	τ_1 (ps)	I_1 (%)	τ_2 (ps)	I_2 (%)
Before thermal treatment	172 ± 1	24.7 ± 0.5	274 ± 2	72.6 ± 0.5
After thermal treatment	171 ± 1	24.5 ± 0.5	274 ± 2	73.0 ± 0.5

3.3. Photoluminescence emissions

Fig. SI-6 shows the PL emission spectra of α-Ag_2WO_4 as a function of temperature (343, 373, 398, and 423 K). It is observed that the α-Ag_2WO_4 emission is centered on two specific peaks, one located at ~460 nm and the other at ~730 nm. The emission in the blue region is related to the transitions from the ground state A_1 to the high $^1T_2$ vibration level that occurs in [WO_6] clusters [34]. Furthermore, these more energetic emissions can be enhanced due to the increase of structural defects in the sample [27]. These structural defects cause the creation of more energetic intermediate levels in the middle of the forbidden region of the band gap (deep defects) [35]. The emission observed in the red region is directly related to the electronic density generated by V_O in the [AgO_x] clusters (x = 2, 4, 6, and 7) which can recombine with the V_{Ag} resulting in changes in these emissions [34]. These alterations cause the formation of less energetic energy levels, close to the valence and conduction bands of the semiconductor (shallow defects). The amount of both types of defects is reduced with increasing temperature, indicating an increase in the structural order of the sample [36]. This effect is in agreement with the Rietveld refinement analyses, where it was possible to observe an increase in the volume of the crystalline cell (see Table SI-1) due to oxygen diffusion into the grains, which decreases the V_O density as shown in PL (Fig. SI-6) [34, 37].

3.4. Impedance spectroscopy

The Nyquist plots (-Z' vs. Z'') of the α-Ag_2WO_4 at different temperatures are shown in Fig. 2. From the figure, a diminution of the semicircle radii with increasing temperature is observed. This behavior can be related to the higher mobility of the charge carriers with temperature, reaching sufficient energy to pass through the barrier when the temperature rises. We can sense that the semicircular arcs are not centered

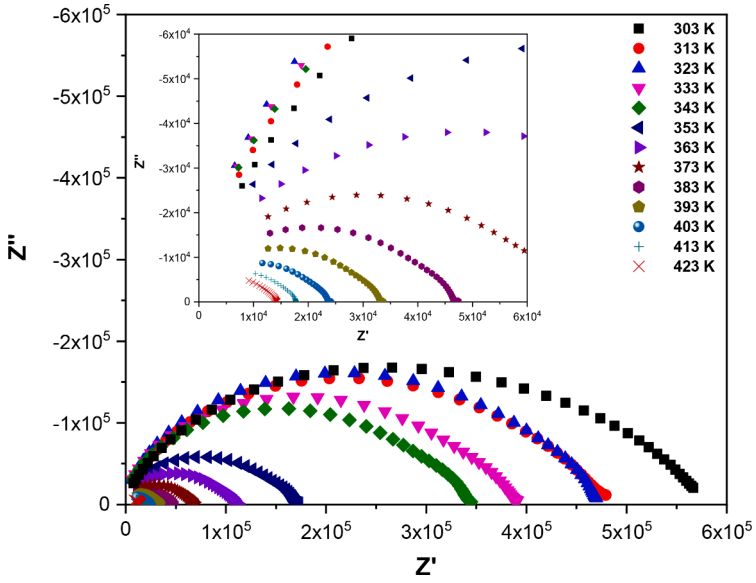

Fig. 2. Nyquist plots (-*Z*' vs. *Z*'') of the α-Ag_2WO_4 pellets at different temperatures.

on the real axis, which means the α-Ag_2WO_4 samples present non-Debye-type relaxation processes. The samples were found to obey the Cole-Cole formalism [38–40]. Generally, each semicircle is attributed to a specific contribution: it represents grain contributions at high frequencies and grain boundaries and electrode contributions at low frequencies which are commonly overlapped. Then, to better perform the analysis of the impedance data, the total parallel equivalent capacitance (C_p) and the total parallel resistance (R_p) as a function of frequency will be analyzed to reveal the electrical conduction mechanisms [41].

For the fitting of the Nyquist plots, an equivalent circuit with a combination of ideal resistors, capacitances, and inductances can be used. Nevertheless, ideal elements only approximate over a limited frequency range. When dealing not with a single activation energy but with a distribution of activation energies, one passes from a simple ideal resistor and capacitor in parallel or series to a distributed impedance element. The disordered states associated with deep bulk defects in semiconductors grains could be the phenomenon that modifies the Debye-like response. Then a better fitting to experiments can be obtained when a large number of different disordered states as RC series are added in parallel to the grain boundary contribution [39].

For the fitting, the equivalent circuit employed in this study is displayed in Fig. 3A, where R_b, C_b, R_e, Ce, and R_{gb}, C_{gb}, R_d, CPE_d represent the resistance and capacitance of the bulk of grains, of the electrodes, and those of grain boundaries, the resistance related to distributed defects and the constant phase element of the defects, respectively [42]. From an electronic point of view, these defects, in turn, display low or high electron density, rendering different charge accumulation.

Particularly, this electrical behavior of states due to distributed defects is modeled by a series combination of resistance (R_d) and a constant phase element (CPE_d). A *CPE* is a simple distributed element that produces an impedance having a constant phase angle in the complex plane according to the Eq. (1):

$$Z_{CPE} = \frac{A}{(j\omega)^{\alpha}} \tag{1}$$

where ω is the angular frequency. Constant A and exponent α correspond to the impedance modulus and impedance angle, respectively. If $\alpha = 1$, the *CPE* acts like a capacitor with A equal to the capacitance. The *CPE* can also behave as a resistance ($\alpha = 0$) or an inductance ($\alpha = -1$) [30, 43].

The total electrical behavior is well represented in R_p and C_p vs. f(Hz)

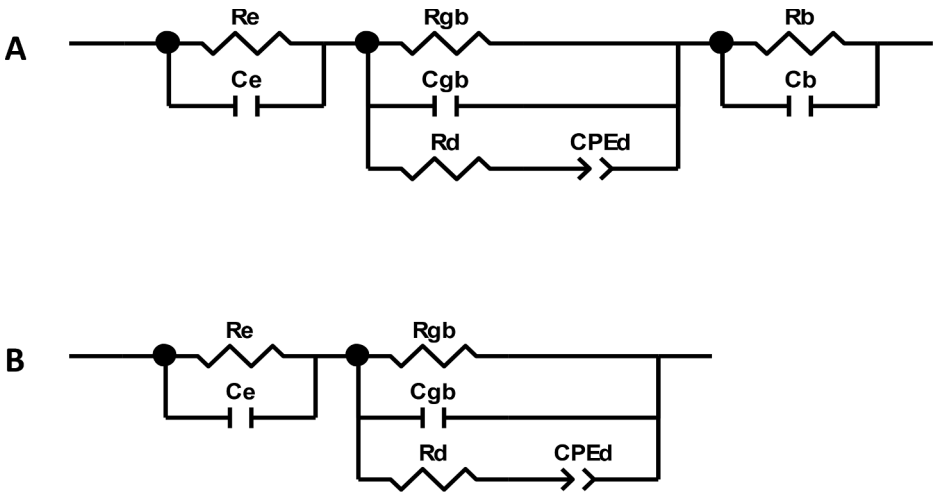

Fig. 3. (A) Complete equivalent circuit. **(B)** Simplified equivalent circuit: for our experimental values, R_b and C_b do not play a relevant role in the whole circuit. Then, we do not take into account the bulk contribution for modeling.

plots, as shown in Fig. 4A and 4B, respectively.

Table 2 indicates the obtained electrical parameter values for fitting. It can be seen that the modeled values of R_e and R_{gb} decrease as temperature increases, which indicates a thermally activated conduction mechanism. Interestingly, R_d increases until 323 K and then decreases, rending a competition between temperature and carrier concentration. From the fittings, we also observed in Table 2 that the electrode capacitance increases with temperature. Fig. SI-7 shows the fitting of the experimental results using the electrical circuit proposed in Fig. 3B from 303 to 423 K. To explain the observed capacitance variation with temperature the electrical currents through the grain boundary are further investigated.

3.5. The electrical currents through the grain boundary

It is widely accepted that the electrical conduction in polycrystalline semiconductors is dominated by intergranular potential barriers that have a Schottky-type nature [41,44–52]. Then, to study the electrical currents, we must first model the observed electrical behavior using an equivalent circuit to obtain the relevant electrical components (Grain Boundary Capacitance C_{gb} and Grain Boundary Resistance R_{gb}).

For the equivalent circuit of Fig. 3B, the values of R_{gb} and C_{gb} can be determined from the limit values of the conductance (G_p) and capacitance (C_p) for very low and very high frequencies (Fig. 4A, B) as [53]:

$$G_{p_{\omega\to 0}} = \frac{1}{R_{gb}} \tag{2}$$

and,

$$C_{p_{\omega\to\infty}} = C_{gb} \tag{3}$$

To study the grain boundary capacitance changes, we can consider the C_{gb} at a frequency of 1 MHz ($C_p \approx C_{gb}$). The procedure used to obtain the values of the electrical grain boundary capacitance and resistance is described in the supplementary part of this article. In particular, for our working frequency, the electrode effects on total impedance and total capacitance can be estimated assuming a quite initial high value for the electrode capacitance (10^{-5} F) for 303 K. Grain boundary resistance (R_{gb}) can be determined at low frequencies, say 100 Hz. The resistance values decrease with the increase in temperature (Fig. 5, Table 2, and Fig. SI-7), which can be explained by the increased mobility of the charge carriers that contribute to the conduction process.

Fig. 5 shows the electrical conductance and capacitance behavior (Fig. 5 inset) of the potential grain boundary barriers analyzed at 100 Hz for the *Gp* curve, and 1 MHz for the *Cp* curve ($Cp = C_{gb}$ at 1 MHz, and $G_p = G_{gb}$ at 100 Hz at a bias of 0 V). The total capacitance dependence on frequency is affected by the presence of bulk defects and the electrodes. These bulk defects have different activation energies reinforcing the use of a constant phase element.

It is known that carriers, with energies below the top of a barrier, can penetrate it by quantum-mechanical tunneling. On the other hand,

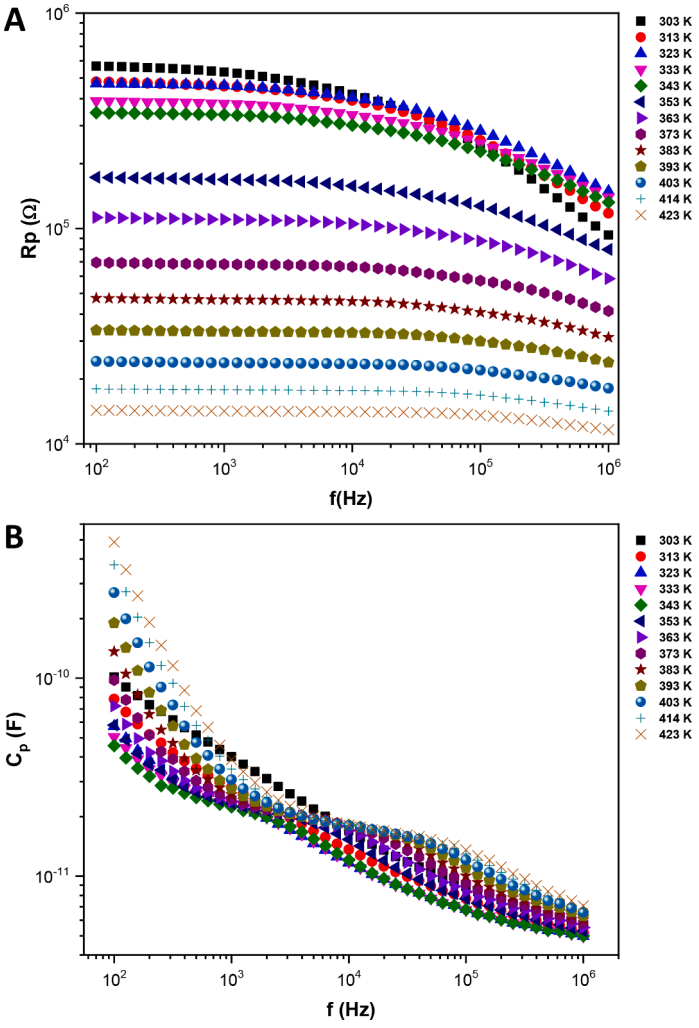

Fig. 4. **(A)** R_p and **(B)** C_p total electrical behavior as a function of frequency (Hz).

Table 2
Experimental grain boundary resistance and capacitance dependence with temperature used for fitting the C_p vs f behaviors are shown in the table. R_{gb} is obtained from total parallel resistance (R_p) at 100 Hz and C_{gb} from total parallel capacitance (C_p) at 1 MHz. From the fitting with the equivalent circuit of Fig. 3B, R_e, C_e, and trap parameters were obtained as a function of the temperature.

T (°C)	R_{gb} (Ω) f:100Hz	C_{gb} (10^{-12}F) f:1MHz	R_e (Ω)	C_e (10^{-8}F)	R_d (Ω)	CPE_d (10^{-10} F)	α
303	567,510	5.06	15,000	8	70,805	121.30	0.61
313	463,790	5.24	11,000	8	163,250	27.54	0.70
323	470,100	4.99	5000	60	273,710	27.54	0.70
333	391,120	5.01	2000	200	269,120	27.54	0.70
343	344,540	4.97	1500	250	261,460	27.54	0.70
353	172,000	5.28	820	300	194,710	12.85	0.78
363	112,530	5.51	700	400	186,260	9.81	0.82
373	69,513	5.80	400	500	142,960	4.92	0.88
383	47,443	6.03	300	500	120,160	5.24	0.88
393	33,690	6.28	250	750	98,293	4.03	0.90
403	24,124	6.56	180	800	77,135	4.81	0.89
413	18,012	6.83	140	1000	62,003	6.02	0.87
423	14,328	7.01	100	1500	69,783	7.82	0.86

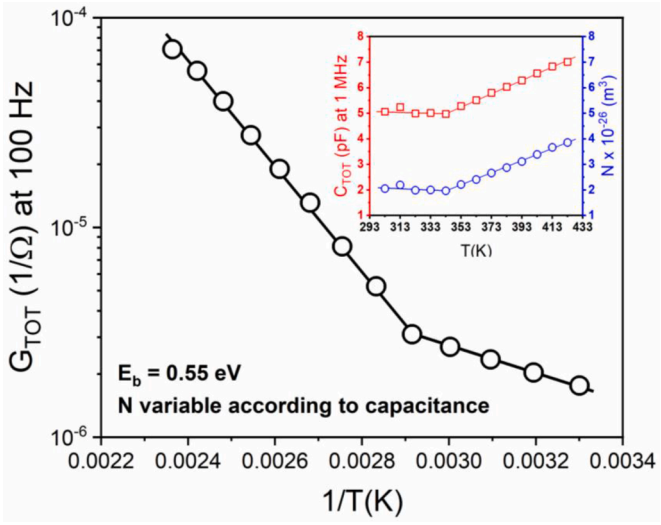

Fig. 5. Electrical conductance (G_p) and capacitance (C_p) behavior (inset) of the potential grain boundary barriers. The net acceptor concentration (N) dependence on temperature is also shown in the inset. G_p values are extracted at 100 Hz from Fig. 4**A** and C_p values are obtained from Fig. 4**B** at 1 MHz (Cp=C_{gb} at 1 MHz, and G_p =G_{gb} at 100 Hz at a bias of 0 V).

carriers can overcome the barrier height (ϕ) to move from one grain to another favoring the thermionic emission Thus, we calculated the two main contributions to electrical conduction, namely, the thermionic emission and the tunneling contribution. The tunneling current can be calculated with Eq. (4):

$$J_{tun} = \frac{A^* T}{k} \int_0^{\phi} F(E)P(E)dE \tag{4}$$

where A* is the Richardson constant, F(E) is the Fermi-Dirac distribution, and P(E) is the transmission probability, which can be determined with the Wentzel-Kramer-Brillouin approximation [54]. For high dopant concentrations, such as the ones found here, thermionic-field emission is the most relevant conduction mechanism. By solving Poisson's equation for the depletion approximation, the relationship between the grain boundary capacitance (C_{gb} or C_p at 1 MHz) and the band bending (V_b) in volts is:

$$C_{gb} = \left[\frac{eN\varepsilon}{V_b - \frac{kT}{e}}\right]^{\frac{1}{2}} \tag{5}$$

where, e is the electron charge, k is the Boltzmann constant, T is the experimental temperature, ε is the permittivity and N, as define above, is the net acceptor concentration.

An analysis of the results of Table 2 renders that in the 303 - 423 K range, the PL emission spectra show that the amount of Vo was reduced when temperature increases and, consequently, the net doping concentration (N) would increase as the temperature is raised. Changes in N directly reflect in the values of C_{gb} as shown in Fig. 5 inset. This result is consistent with the slight increase in the lattice parameters detected during Rietveld refinements (see Section 3.3). The increase of the values for the capacitance (C_e) with temperature could be a consequence of the short-distance oxygen diffusion into the grains that are directly in contact with the electrodes. Also, for R_d and CPE_d we have to consider the effect of temperature and the Fermi level position on the activated process rate of trap charging (as shown in the band diagram of Fig. SI-5). As a consequence, R_d and CPE_d can increase or decrease with temperature as observed in Table 2.

The fitting shown in Fig. 5 was obtained with an iterative process for a constant band bending of E_b=eV_b=0.55 eV and a variable doping according to capacitance changes, considering an $N = 2 \times 10^{25}$ m^{-3} for the low temperatures. The doping was determined considering that the capacitance is directly related to the square root of the doping, which is the case for parabolic barriers. The values derived from the iterative process depend on the temperature and are those shown in the inset of Fig. 5. Note that the observed trend of the total conductance changes at about 343 K, and it is directly correlated with the increase of the grain boundary capacitance.

4. Conclusions

Understanding the relationships among the structure, nature of defects and the electrical transport is essential for designing semiconductors with multifunctional properties. Here, α-Ag_2WO_4 samples were synthesized via a simple CP method, and their physicochemical properties were characterized by a wide range of techniques: XRD with Rietveld refinements, FE-SEM images, impedance spectroscopy, PALS, and PL emissions.

The main conclusions of the present work can be summarized as follows: (i) α-Ag_2WO_4 present cationic (oxygen vacancies, V_O), and anionic (Ag-O vacancy-complexes) vacancies with Schottky p-type potential barriers at grain boundaries (with defects accumulation on the grain surface), (ii) during the thermal treatment on the α-Ag_2WO_4 polycrystals, the defect structure type (Ag–O vacancy-complexes) remains constant, (iii) the relationship between the results of PL emissions and impedance spectroscopy shows that the density oxygen vacancies, V_O, decreases when temperature increases and, consequently, the net doping concentration would increase as the temperature is raised. This result is consistent with the slight increase of the lattice parameters

measured during Rietveld refinements, (iv) when the polycrystalline α-Ag_2WO_4 semiconductor is exposed to an air atmosphere, at temperatures greater than 423 K, there is an annihilation of oxygen vacancies, Vo, without appreciable changes in the concentration of the Ag-O vacancy-complexes, and (v) the good fitting of the conductivity as a function of temperature gives confidence on the proposed tunneling plus thermionic conduction mechanisms. Overall, the results advance the understanding of p-type Ag_2WO_4 semiconductors, which provides a platform for controllable synthesis with desired functional properties for technological applications.

CRediT authorship contribution statement

M. Assis: Investigation, Methodology, Formal analysis, Conceptualization, Data curation, Writing – original draft, Writing – review & editing. **M.S. Castro:** Conceptualization, Data curation, Writing – original draft, Writing – review & editing. **C.M. Aldao:** Funding acquisition, Resources, Conceptualization, Data curation, Writing – original draft, Writing – review & editing. **C. Buono:** Conceptualization, Data curation, Writing – original draft. **P.P. Ortega:** Methodology, Formal analysis. **M. D. Teodoro:** Methodology, Formal analysis. **J. Andrés:** Funding acquisition, Resources, Conceptualization, Data curation, Writing – original draft, Writing – review & editing. **A.F. Gouveia:** Writing – original draft, Writing – review & editing. **A.Z. Simões:** Methodology, Formal analysis. **E. Longo:** Funding acquisition, Resources, Conceptualization, Data curation, Writing – original draft, Writing – review & editing. **C.E. Macchi:** Conceptualization, Data curation, Writing – original draft, Writing – review & editing. **A. Somoza:** Funding acquisition, Resources, Conceptualization, Data curation, Writing – original draft, Writing – review & editing. **F. Moura:** Methodology, Formal analysis. **M.A. Ponce:** Funding acquisition, Resources, Conceptualization, Data curation, Writing – original draft, Writing – review & editing.

Declaration of Competing Interest

The authors declare that they have no known competing financial interests or personal relationships that could have appeared to influence the work reported in this paper.

Acknowledgments

This work was funded in part by Fundação de Amparo à Pesquisa do Estado de São Paulo - FAPESP (2013/07296-2), Conselho Nacional de Desenvolvimento Científico e Tecnológico – CNPq, Financiadora de Estudos e Projetos – FINEP, and Coordenação de Aperfeiçoamento de Pessoal de Nível Superior – CAPES (001). M.A. was supported by the Margarita Salas postdoctoral contract MGS/2021/21 (UP2021-021) financed by the European Union-Next Generation EU. A.F.G. would like to acknowledge the funding received from the Universitat Jaume I through its Research Stay Grants (E-2022-05) and for the postdoctoral contract (POSDOC/2019/30), and FAPESP (2019/01732-1). J.A acknowledges Universitat Jaume I (project UJI-B2019-30), and the Ministerio de Ciencia, Innovación y Universidades (Spain) (project PGC2018094417-B-I00) for financially supporting this research. C.M. A, M.A.P, C.B and M.S.C would like to acknowledge ANPCyT (Agencia Nacional de Promoción Científica y Tecnológica, Argentina) and CONICET.

Supplementary materials

Supplementary material associated with this article can be found, in the online version, at doi:10.1016/j.materresbull.2023.112252.

References

[1] F.C. Tompkins, Superficial chemistry and solid imperfections, Nature 186 (1960) 3–6, https://doi.org/10.1038/186003a0.
[2] C.J. Kevane, Oxygen vacancies and electrical conduction in metal oxides, Phys. Rev. 133 (1964) A1431, https://doi.org/10.1103/PhysRev.133.A1431.
[3] S.T. Pantelides, The electronic structure of impurities and other point defects in semiconductors, Rev. Mod. Phys. 50 (1978) 797, https://doi.org/10.1103/RevModPhys.50.797.
[4] R. Waser, M. Aono, Nanoionics-based resistive switching memories, Nat. Mater. 611 (6) (2007) 833–840, https://doi.org/10.1038/nmat2023, 2007.
[5] A. Alkauskas, M.D. McCluskey, C.G. Van de Walle, Tutorial: defects in semiconductors-combining experiment and theory, J. Appl. Phys. 119 (2016), 181101, https://doi.org/10.1063/1.4948245.
[6] F. Gunkel, D.V. Christensen, Y.Z. Chen, N. Pryds, Oxygen vacancies: the (in)visible friend of oxide electronics, Appl. Phys. Lett. 116 (2020), 120505, https://doi.org/10.1063/1.5143309.
[7] C.T. Campbell, C.H.F. Peden, Oxygen vacancies and catalysis on ceria surfaces, Science 309 (2005) 713–714, https://doi.org/10.1126/SCIENCE.1113955.
[8] F. Li, Y. Hou, Z. Yu, L. Qian, L. Sun, J. Huang, Q. Ran, R. Jiang, Q. Sun, H. Zhang, Oxygen deficiency introduced to Z-scheme CdS/WO_{3-x} nanomaterials with MoS_2 as the cocatalyst towards enhancing visible-light-driven hydrogen evolution, Nanoscale 11 (2019) 10884–10895, https://doi.org/10.1039/C8NR10230A.
[9] M. Sachs, J.S. Park, E. Pastor, A. Kafizas, A.A. Wilson, L. Francàs, S. Gul, M. Ling, C. Blackman, J. Yano, A. Walsh, J.R. Durrant, Effect of oxygen deficiency on the excited state kinetics of WO_3 and implications for photocatalysis, Chem. Sci. 10 (2019) 5667–5677, https://doi.org/10.1039/C9SC00693A.
[10] L. Ji, B. Li, X. Xu, F. Wang, Oxygen deficiencies and metallic Bi-mediated photocatalytic activity of bismuth tungsten oxides, Appl. Surf. Sci. 463 (2019) 872–878, https://doi.org/10.1016/J.APSUSC.2018.09.011.
[11] A. Kumar, M. Kumar, V. Navakoteswara Rao, M.V. Shankar, S. Bhattacharya, V. Krishnan, Unraveling the structural and morphological stability of oxygen vacancy engineered leaf-templated $CaTiO_3$ towards photocatalytic H_2 evolution and N_2 fixation reactions, J. Mater. Chem. A 9 (2021) 17006–17018, https://doi.org/10.1039/D1TA04180K.
[12] A. Kumar, V. Krishnan, Vacancy engineering in semiconductor photocatalysts: implications in hydrogen evolution and nitrogen fixation applications, Adv. Funct. Mater. 31 (2021), 2009807, https://doi.org/10.1002/ADFM.202009807.
[13] K. Hoang, M. Oh, Y. Choi, Electronic structure, polaron formation, and functional properties in transition-metal tungstates, RSC Adv. 8 (2018) 4191–4196, https://doi.org/10.1039/C7RA13436C.
[14] Y.V.B. De Santana, J.E.C. Gomes, L. Matos, G.H. Cruvinel, A. Perrin, C. Perrin, J. Andrès, J.A. Varela, E. Longo, Silver molybdate and silver tungstate nanocomposites with enhanced photoluminescence, Nanomater. Nanotechnol. 4 (2014) 22, https://doi.org/10.5772/58923.
[15] A. Sreedevi, K.P. Priyanka, S.C. Vattappalam, T. Varghese, Silver tungstate nanoparticles for the detection of ethanol, ammonia and acetone gases, J. Electron. Mater. 47 (2018) 6328–6333, https://doi.org/10.1007/S11664-018-6551-8.
[16] M. Assis, T. Robeldo, C.C. Foggi, A.M. Kubo, G. Mínguez-Vega, E. Condoncillo, H. Beltran-Mir, R. Torres-Mendieta, J. Andrés, M. Oliva, C.E. Vergani, P. A. Barbugli, E.R. Camargo, R.C. Borra, E. Longo, Ag nanoparticles/α-Ag_2WO_4 composite formed by electron beam and femtosecond irradiation as potent antifungal and antitumor agents, Sci. Rep. 9 (2019) 9927, https://doi.org/10.1038/s41598-019-46159-y.
[17] M. Assis, E. Cordoncillo, R. Torres-Mendieta, H. Beltrán-Mir, G. Mínguez-Vega, R. Oliveira, E.R. Leite, C.C. Foggi, C.E. Vergani, E. Longo, J. Andrés, Towards the scale-up of the formation of nanoparticles on α-Ag_2WO_4 with bactericidal properties by femtosecond laser irradiation, Sci. Rep. 8 (2018) 1884, https://doi.org/10.1038/s41598-018-19270-9.
[18] K. Nubla, N. Sandhyarani, Ag nanoparticles anchored Ag_2WO_4 nanorods: an efficient methanol tolerant and durable Pt free electro-catalyst toward oxygen reduction reaction, Electrochim. Acta 340 (2020), 135942, https://doi.org/10.1016/J.ELECTACTA.2020.135942.
[19] N.G. Macedo, A.F. Gouveia, R.A. Roca, M. Assis, L. Gracia, J. Andrés, E.R. Leite, E. Longo, Surfactant-mediated morphology and photocatalytic activity of α-Ag_2WO_4 material, J. Phys. Chem. C 122 (2018) 8667–8679, https://doi.org/10.1021/acs.jpcc.8b01898.
[20] M.V.B. do Nascimento, F.X. Nobre, E.N.D. de Araújo, C.I.L. de Araújo, P.R. C. Couceiro, L. Manzato, $Ag_{2-x}Cu_xWO_4$ solid solution: structure, morphology, optical properties, and photocatalytic performance in the degradation of RhB under blue light-emitting device irradiation, J. Phys. Chem. C 125 (2021) 11875–11890, https://doi.org/10.1021/ACS.JPCC.1C00099.
[21] W.D.S. Pereira, M.M. Ferrer, G. Botelho, L. Gracia, I.C. Nogueira, I.M. Pinatti, I.L. V. Rosa, F.D.A. La Porta, J. Andrés, E. Longo, Effects of chemical substitution on the structural and optical properties of α-$Ag_{2-2x}Ni_xWO_4$ ($0 \leq x \leq 0.08$) solid solutions, Phys. Chem. Chem. Phys. 18 (2016) 21966–21975, https://doi.org/10.1039/c6cp00575f.
[22] P.F.S. Pereira, C.C. Santos, A.F. Gouveia, M.M. Ferrer, I.M. Pinatti, G. Botelho, J. R. Sambrano, I.L.V. Rosa, J. Andrés, E. Longo, α-$Ag_{2-2x}Zn_xWO_4$ ($0 \leq x \leq 0.25$) solid solutions: structure, morphology, and optical properties, Inorg. Chem. 56 (2017) 7360–7372, https://doi.org/10.1021/acs.inorgchem.7b00201.
[23] M.D.P. Silva, R.F. Gonçalves, I.C. Nogueira, V.M. Longo, L. Mondoni, M.G. Moron, Y.V. Santana, E. Longo, Microwave-assisted hydrothermal synthesis of $Ag_2(W_{1-x}Mo_x)O_4$ heterostructures: nucleation of Ag, morphology, and photoluminescence properties, Spectrochim. Acta Part A Mol. Biomol. Spectrosc. 153 (2016) 428–435, https://doi.org/10.1016/J.SAA.2015.08.047.

[24] M.D. Penha, A.F. Gouveia, M.M. Teixeira, R.C. de Oliveira, M. Assis, J. R. Sambrano, F. Yokaichya, C.C. Santos, R.F. Gonçalves, M.S. Li, M.A. San-Miguel, J. Andrés, E. Longo, Structure, optical properties, and photocatalytic activity of α-$Ag_2W_{0.75}Mo_{0.25}O_4$, Mater. Res. Bull. 132 (2020), 111011, https://doi.org/10.1016/j.materresbull.2020.111011.
[25] I.M. Pinatti, P.F.S. Pereira, M. de Assis, E. Longo, I.L.V. Rosa, Rare earth doped silver tungstate for photoluminescent applications, J. Alloy. Compd. 771 (2019) 433–447, https://doi.org/10.1016/j.jallcom.2018.08.302.
[26] I.M. Pinatti, I.C. Nogueira, W.S. Pereira, P.F.S. Pereira, R.F. Gonçalves, J.A. Varela, E. Longo, I.L.V. Rosa, Structural and photoluminescence properties of Eu^{3+} doped α-Ag_2WO_4 synthesized by the green coprecipitation methodology, Dalton Trans. 44 (2015) 17673–17685, https://doi.org/10.1039/c5dt01997d.
[27] M. Assis, M.A. Ponce, A.F. Gouveia, D. Souza, J.P. de Campos da Costa, V. Teodoro, Y.G. Gobato, J. Andrés, C. Macchi, A. Somoza, E. Longo, Revealing the nature of defects in α-Ag_2WO_4 by positron annihilation lifetime spectroscopy: a joint experimental and theoretical study, Cryst. Growth Des. 21 (2021) 1093–1102, https://doi.org/10.1021/acs.cgd.0c01417.
[28] J. Kansy, Microcomputer program for analysis of positron annihilation lifetime spectra, Nucl. Instrum. Methods Phys. Res. Sect. A Accel. Spectrom. Detect. Assoc. Equip. 374 (1996) 235–244, https://doi.org/10.1016/0168-9002(96)00075-7.
[29] E. Von Hauff, Impedance spectroscopy for emerging photovoltaics, J. Phys. Chem. C 123 (2019) 11329–11346, https://doi.org/10.1021/ACS.JPCC.9B00892.
[30] J.R. MacDonald, W.R. Kenan, Impedance Spectroscopy: Emphasizing Solid Materials and Systems, 1st ed., John Wiley & Sons, 1987.
[31] L.H. da S. Lacerda, E. Longo, J. Andrés, M.A. San-Miguel, A diagnosis approach for semiconductor properties evaluation from ab initio calculations: Ag-based materials investigation, J. Solid State Chem. 305 (2022), 122670, https://doi.org/10.1016/j.jssc.2021.122670.
[32] H.E. Schaefer, R. Würschum, R. Birringer, H. Gleiter, Structure of nanometer-sized polycrystalline iron investigated by positron lifetime spectroscopy, Phys. Rev. B 38 (1988) 9545–9554, https://doi.org/10.1103/PhysRevB.38.9545.
[33] I. Makkonen, E. Korhonen, V. Prozheeva, F. Tuomisto, Identification of vacancy defect complexes in transparent semiconducting oxides ZnO, In_2O_3 and SnO_2, J. Phys. Condens. Matter 28 (2016), 224002, https://doi.org/10.1088/0953-8984/28/22/224002.
[34] M. Assis, R.A. Pontes Ribeiro, M.H. Carvalho, M.M. Teixeira, Y.G. Gobato, G. A. Prando, C.R. Mendonça, L. de Boni, A.J. Aparecido de Oliveira, J. Bettini, J. Andrés, E. Longo, Unconventional magnetization generated from electron beam and femtosecond irradiation on α-Ag_2WO_4: a quantum chemical investigation, ACS Omega 5 (2020) 10052–10067, https://doi.org/10.1021/acsomega.0c00542.
[35] L.S. Cavalcante, M.A.P. Almeida, W. Avansi, R.L. Tranquilin, E. Longo, N.C. Batista, V.R. Mastelaro, M.S. Li, Cluster coordination and photoluminescence properties of α-Ag_2WO_4 microcrystals, Inorg. Chem. 51 (2012) 10675–10687, https://doi.org/10.1021/ic300948n.
[36] L.O. Laier, M. Assis, C.C. Foggi, A.F. Gouveia, C.E. Vergani, L.C.L. Santana, L. S. Cavalcante, J. Andrés, E. Longo, Surface-dependent properties of α-Ag_2WO_4: a joint experimental and theoretical investigation, Theor. Chem. Acc. 139 (2020) 108, https://doi.org/10.1007/s00214-020-02613-z.
[37] L. Cruz, M.M. Teixeira, V. Teodoro, N. Jacomaci, L.O. Laier, M. Assis, N.G. Macedo, A.C.M. Tello, L.F. da Silva, G.E. Marques, M.A. Zaghete, M.D. Teodoro, E. Longo, Multi-dimensional architecture of Ag/α-Ag_2WO_4 crystals: insights into microstructural, morphological, and photoluminescence properties, CrystEngComm 22 (2020) 7903–7917, https://doi.org/10.1039/D0CE00876A.
[38] H. Rahmouni, A. Benali, B. Cherif, E. Dhahri, M. Boukhobza, K. Khirouni, M. Sajieddine, Structural and electrical properties of $Zn_{1-x}Ni_xFe_2O_4$ ferrite, Phys. B Condens. Matter 466-467 (2015) 31–37, https://doi.org/10.1016/J.PHYSB.2015.03.019.
[39] J.R. Macdonald, W.B. Johnson, Fundamentals of Impedance Spectroscopy, in: E. Barsoukov, J.R. Macdonald (Eds.), Impedance Spectroscopy: Theory, Experiment, and Applications, John Wiley & Sons, Inc, New Jersey, 2005, pp. 1–26, https://doi.org/10.1002/0471716243.ch1.
[40] U. Intatha, S. Eitssayeam, J. Wang, T. Tunkasiri, Impedance study of giant dielectric permittivity in $BaFe_{0.5}Nb_{0.5}O_3$ perovskite ceramic, Curr. Appl. Phys. 10 (2010) 21–25, https://doi.org/10.1016/J.CAP.2009.04.006.
[41] C. Malagù, M.C. Carotta, A. Giberti, V. Guidi, G. Martinelli, M.A. Ponce, M. S. Castro, C.M. Aldao, Two mechanisms of conduction in polycrystalline SnO_2, Sens. Actuators B Chem. 136 (2009) 230–234, https://doi.org/10.1016/J.SNB.2008.10.015.
[42] V.F. Lvovich, Equivalent-circuit elements and modeling of the impedance phenomenon, Impedance Spectrosc. (2012) 37–47, https://doi.org/10.1002/9781118164075.CH3.
[43] J. Zimmermann, U. van Rienen, Ambiguity in the interpretation of the low-frequency dielectric properties of biological tissues, Bioelectrochemistry 140 (2021), 107773, https://doi.org/10.1016/J.BIOELECHEM.2021.107773.
[44] M.A. Ponce, P.R. Bueno, J. Varela, M.S. Castro, C.M. Aldao, Impedance spectroscopy analysis of SnO_2 thick-films gas sensors, J. Mater. Sci. Mater. Electron. 1912 (19) (2007) 1169–1175, https://doi.org/10.1007/S10854-007-9517-9, 2007.
[45] Madou, M., Morrison, S.R. Chemical sensing with solid state devices, in: 1989.
[46] G.D. Mahan, L.M. Levinson, H.R. Philipp, Theory of conduction in ZnO varistors, J. Appl. Phys. 50 (1979) 2799–2812, https://doi.org/10.1063/1.326191.
[47] G.E. Pike, Semiconductor grain-boundary admittance: theory, Phys. Rev. B 30 (1984) 795–802, https://doi.org/10.1103/PhysRevB.30.795.
[48] A. Gurlo, N. Bârsan, M. Ivanovskaya, U. Weimar, W. Göpel, In_2O_3 and MoO_3–In_2O_3 thin film semiconductor sensors: interaction with NO_2 and O_3, Sens. Actuators B Chem. 47 (1998) 92–99, https://doi.org/10.1016/S0925-4005(98)00033-1.
[49] N. Yamazoe, Toward innovations of gas sensor technology, Sens. Actuators B Chem. 108 (2005) 2–14, https://doi.org/10.1016/j.snb.2004.12.075.
[50] M. Batzill, U. Diebold, The surface and materials science of tin oxide, Prog. Surf. Sci. 79 (2005) 47–154, https://doi.org/10.1016/j.progsurf.2005.09.002.
[51] D.R. Leite, M. Cilense, M.O. Orlandi, P.R. Bueno, E. Longo, J.A. Varela, The effect of TiO_2 on the microstructural and electrical properties of low voltage varistor based on $(Sn,Ti)O_2$ ceramics, Phys. Status Solidi 207 (2010) 457–461, https://doi.org/10.1002/pssa.200925304.
[52] C. Buono, F. Schipani, M.A. Ponce, C.M. Aldao, Intergranular barrier height fluctuations in polycrystalline semiconductors, Phys. Status Solidi C 14 (2017), 1700069, https://doi.org/10.1002/pssc.201700069.
[53] M.A. Ponce, M.A. Ramírez, R. Parra, C. Malagú, M.S. Castro, P.R. Bueno, J. A. Varela, Influence of degradation on the electrical conduction process in ZnO and SnO_2-based varistors, J. Appl. Phys. 108 (2010), 074505, https://doi.org/10.1063/1.3490208.
[54] C. Buono, D.A. Mirabella, C.M. Aldao, Sensitivity of metal oxide gas sensors to non-parabolic intergranular barriers, Sens. Actuators B Chem. 246 (2017) 1025–1029, https://doi.org/10.1016/j.snb.2017.02.146.